



A novel approach for immobilizing Ag/ZnO nanorods on a glass substrate: Application in solar light-driven degradation of micropollutants in water

Yanan Li ^a, Isaac Sánchez-Montes ^b, Lingling Yang ^b, Mohamed Gamal El-Din ^{b,*}, Xuehua Zhang ^{a,*}

^a Department of Chemical and Materials Engineering, University of Alberta, Edmonton, AB T6G 1H9, Canada

^b Department of Civil and Environmental Engineering, University of Alberta, Edmonton, AB T6G 1H9, Canada

ARTICLE INFO

Keywords:

Immobilized photocatalyst
ZnO nanorods
Silver deposition
Solar radiation
Organic contaminants

ABSTRACT

One of the main challenges in applying photocatalysts for water treatment is the complex separation and recycling process. In this study, we developed highly stable, porous zinc oxide nanorods (ZnO NRs) immobilized on glass vials using a solvent exchange process (SEP) and hydrothermal calcination. Key parameters, including oleic acid concentration and hydrothermal growth time, were optimized to maximize the active surface area, significantly enhancing photodegradation performance. Under the best conditions, ZnO NRs-coated vials achieved nearly 100% degradation of sulfamethoxazole (SMX) in 10 h of simulated solar irradiation. Depositing silver nanoparticles on the surface of ZnO NRs (Ag/ZnO NRs) further improved performance, reducing degradation time to 4 h and increasing photocatalyst stability. The Ag/ZnO NRs-coated vials, optimized with an Ag precursor concentration of 0.05 M, also demonstrated high degradation rates (>99%) for eight organic micropollutants at environmentally relevant concentrations over multiple reuse cycles and with minimal metal leaching. This study presents an innovative, tunable method for immobilizing photocatalysts on glass substrates, offering high surface area, excellent photocatalytic activity, and mechanical properties, making it highly suitable for water treatment applications.

1. Introduction

The increasing global concern over the presence of micropollutants (MPs) in water bodies has driven extensive research towards the development of efficient decontamination technologies. MPs, including pharmaceuticals, pesticides, and personal care products, are frequently detected in water bodies worldwide, yet their persistence and potential adverse effects on both human health and aquatic life make their removal an important environmental challenge (van Dijk et al., 2023; Qiu et al., 2024; Singh et al., 2024; Xu et al., 2021). Unfortunately, conventional water treatment processes are generally inadequate for the complete degradation of these compounds, demanding the investigation of advanced treatment methods (Li et al., 2022a; Sher et al., 2021).

Advanced oxidation processes (AOPs) are efficient methods to degrade and mineralize a wide range of MPs in water by generating reactive oxygen species (ROS) *in-situ*, such as hydroxyl radicals ($\cdot\text{OH}$), sulfate radicals ($\cdot\text{SO}_4^-$), superoxide radicals ($\cdot\text{O}_2^-$), singlet oxygen ($^1\text{O}_2$), and others (Li et al., 2024; Kim et al., 2024; Lin et al., 2022; Dong et al., 2022; Su et al., 2024; Zhang et al., 2019a). Among the various AOPs, solar-driven catalysis has emerged as a promising strategy due to its efficiency, cost-effectiveness, and sustainable approach (Xie et al.,

2023; Cheng et al., 2023; Tang et al., 2022; Yang et al., 2019; Guo et al., 2023). Photocatalysis effectiveness is based on the ability of a semiconductor to generate ROS through electron-hole (e^-/h^+) pairs upon light irradiation (Yang et al., 2023; Alansi et al., 2022; Yuan et al., 2022). Photogenerated h^+ oxidizes water molecules or hydroxyl ions to produce $\cdot\text{OH}$, while photoexcited e^- reduces adsorbed molecular oxygen to generate $\cdot\text{O}_2^-$ (Rodríguez-González et al., 2020; Luo et al., 2023).

Zinc oxide (ZnO) has been extensively studied as a photocatalyst due to its favorable band gap energy ($E_g = 3.37$ eV), chemical stability, and cost-effectiveness (Ramasamy et al., 2021; Ahmad et al., 2020). However, pure ZnO has limitations, such as the recombination of e^-/h^+ pair and susceptibility to photocorrosion, which reduces its photocatalytic efficiency (Mirzaei et al., 2018b; Lee et al., 2016; Fatima et al., 2022). To overcome these drawbacks, the combination of ZnO with noble metals such as silver (Ag) has been proposed (Ramasamy et al., 2021; Vinh et al., 2021; Ahmad et al., 2022). Research has shown that Ag deposition significantly enhances the photocatalytic performance of ZnO under solar irradiation by increasing charge separation, extending the light absorption range, and providing additional reactive sites for pollutant degradation (Mahrsi et al., 2023; Buengkitcharoen et al.,

* Corresponding authors.

E-mail addresses: mgamalel-din@ualberta.ca (M.G. El-Din), xuehua.zhang@ualberta.ca (X. Zhang).

2023; Zhang et al., 2019b; Wang et al., 2021; Li et al., 2021a; Guo et al., 2022; Pham et al., 2020).

Most studies on ZnO-based photocatalysts have focused on the formation of ZnO nanoparticles in suspension (Zhang et al., 2022a; El Golli et al., 2021; Li et al., 2021b). Although these offer a large surface area that facilitates efficient mass transfer, they are complex to recover from the treated solution (Le et al., 2022; Vaiano and Iervolino, 2018; Zandsalimi et al., 2022). Therefore, immobilizing photocatalysts on substrates is also crucial for practical applications, as it allows for easy recovery and reuse, reducing the operational costs and environmental impact of the treatment process (Le et al., 2022; Rana et al., 2022; Maeng et al., 2015). During the immobilization process, a wide range of ZnO nanostructures could be obtained by tuning the synthesis parameters in hydrothermal, sol-gel, spin-coating, and dip-coating processes, such as films, rods, spheres, and others (Ghos et al., 2021; Luo et al., 2020b; Deebansok et al., 2021; Luo et al., 2020a). Compared to the immobilized ZnO nanoparticles and nanofilms, immobilized ZnO nanorods (NRs) exhibit higher loading amounts and surface area to volume ratio, which increases the photocatalytic degradation efficiency of immobilized ZnO (Zhang et al., 2022b). In addition, NRs structure improves electrical conductivity, charge transfer, carrier mobility, and light absorption efficiency (Mohammed et al., 2020).

This study proposes a novel method to immobilize Ag/ZnO nanorods (Ag/ZnO NRs) on the inner surface of a glass container using a combination of solvent exchange process (SEP) and hydrothermal method. The structural and morphological properties of the fabricated materials were extensively characterized as a function of the conditions in the SEP and hydrothermal treatment time, and their photocatalytic activities were evaluated by degrading a mixture of eight MPs under simulated solar light (SSL). Finally, the re-usability of the coated vials was investigated through several photodegradation cycles, and metal leaching was examined.

2. Materials and methods

2.1. Materials and chemicals

Zinc acetate dihydrate ($\text{Zn}(\text{CH}_3\text{COO})_2 \cdot 2\text{H}_2\text{O}$, 97%) and silver nitrate (AgNO_3 , 0.1 N) were purchased from Fisher Science. Zinc nitrate hexahydrate ($\text{Zn}(\text{NO}_3)_2 \cdot 6\text{H}_2\text{O}$, 98%), hexamethylenetetramine (HMTA, $(\text{CH}_2)_6\text{N}_4$, ≥ 99%), octadecyltrichlorosilane (OTS, 95%) and the MPs, including atrazine (ATZ, $\text{C}_8\text{H}_{14}\text{ClN}_5$, ≥ 98%), caffeine (CAF, $\text{C}_8\text{H}_{10}\text{N}_4\text{O}_2$, 99%), carbamazepine (CBZ, $\text{C}_{15}\text{H}_{12}\text{N}_2\text{O}$, ≥ 98.5%), gemfibrozil (GBZ, $\text{C}_{15}\text{H}_{22}\text{O}_3$, ≥ 99%), ibuprofen (IBF, $\text{C}_{13}\text{H}_{18}\text{O}_2$, 98%), naproxen (NPX, $\text{C}_{14}\text{H}_{14}\text{O}_3$, ≥ 98.5%), sulfamethoxazole (SMX, $\text{C}_{10}\text{H}_{11}\text{N}_3\text{O}_3\text{S}$, ≥ 98%), and trimethoprim (TMP, $\text{C}_{14}\text{H}_{18}\text{N}_4\text{O}_3$, ≥ 98%) were acquired from Sigma-Aldrich. 5,5-Dimethyl-1-pyrroline *N*-oxide (DMPO, $\text{C}_6\text{H}_{11}\text{NO}$, 99%) was purchased from Dojindo Laboratories and 3,4-dihydro-2-methyl-1,1-dimethylethyl ester-2H-pyrrole-2-carboxylic acid-1-oxide (BMPO, $\text{C}_{10}\text{H}_{17}\text{NO}_3$, ≥ 98%) was purchased from Cayman Chemical. All chemicals were used without any further purification. Ultra-pure water (Millipore Milli-Q system, $\rho \geq 18.2 \text{ M}\Omega \text{ cm}$) was employed for solutions preparation.

2.2. Immobilization of ZnO-NRs on the inner surface of glass vials

Hydrophobization pre-treatment: 30 mL glass vials capacity were first cleaned with a 3:1 $\text{H}_2\text{SO}_4:\text{H}_2\text{O}_2$ solution to remove any organic matter from the inner surface, followed by several washings with ultra-pure water. The vials were then hydrophobized with octadecyltrichlorosilane (OTS vials) as described elsewhere (Zhang et al., 2015).

Immobilization of ZnO nanoseeds (ZnO NSs) on OTS vials: ZnO NSs were grown inside pre-hydrophobized glass vials using a SEP, as shown in Fig. 1(a). In step 1, the OTS vial was filled with solution A (oleic acid in ethanol/water 70:30 V/V). Subsequently, solution B

(water) was injected into the vertically oriented vial reactor at a 4 mL/min fixed flow rate through a tube at its center. The total volume of solution B used for the SEP was 60 mL. During this process, oleic acid droplets were formed on the inner surface of the vial due to the oversaturation of oleic acid in the mixture. Next, 30 mL of 0.05 M zinc acetate aqueous solution were added into the vial at a 4 mL/min rate, reacting with the oleic acid droplets and forming zinc oleate nanoparticles. Finally, the vial was rinsed with deionized water and annealed at 500 °C for 2 h to complete the immobilization of the ZnO-NS layer.

Growing of ZnO NRs: ZnO NRs were grown on the pre-seeded inner surface of vials using a wet chemical process. The growth solution was prepared by mixing aqueous solutions of 0.04 M zinc nitrate and 0.04 M HMTA, which had been stirred for 15 min in a 1:1 volume ratio. After an additional 10 min of stirring for homogenization, the pre-seeded vials were filled with the growth solution and maintained at 90 °C for specified duration periods (2, 4, 6, 8, or 10 h), as shown in step 2 of Fig. 1(a). Subsequently, the vials were rinsed with deionized water and dried using airflow before a final annealing process at 500 °C for 3 h to stabilize the material structure.

2.3. Synthesis of Ag/ZnO NRs

Step 3 in Fig. 1(a) shows the process for preparing ZnO NRs with Ag nanoparticles. ZnO NRs-coated vials were filled with aqueous AgNO_3 solutions at different concentrations (0.01, 0.03, 0.05, 0.07, and 0.1 M) and kept in dark conditions for 1 h to allow for adsorption. After this period, the vials were washed with deionized water and dried using airflow. Next, to photoreduce Ag^+ to zerovalent Ag, each vial was exposed to UV irradiation for 30 min using a UVA lamp (365 nm, 8 W, Analytikjena) (Liu et al., 2015). The resultant Ag/ZnO NRs-coated vials were then rinsed several times with deionized water to remove residual Ag^+ ions and dried overnight at room temperature.

2.4. Characterization

Optical images of the ZnO NSs and ZnO NRs were captured using a Nikon H6001 microscope equipped with a Nikon DSFi 3 camera. Powder X-ray diffraction (XRD) analysis was performed with a Bruker D8 Discover diffractometer ($\text{CuK}\alpha$ 1.5406 Å) to determine the structural properties. X-ray photoelectron spectroscopy (XPS) analysis was conducted to assess the material purity and examine the composition and defect characteristics using a PHI 5000 Versa Probe III spectrometer. Monochromatic Al $\text{K}\alpha$ ($h\nu = 1486.6 \text{ eV}$) served as the X-ray source, and the base pressure in the analysis chamber was maintained at 3.0×10^{-10} . The Au 4f_{7/2} peak at 84.0 eV was used to calibrate each spectrum. A pass energy of 224 eV was applied for survey scans, while 26 eV was used for high-resolution spectra. In the XPS spectra, all binding energies were calibrated using the carbon peak (284.8 eV) as the reference. Morphological analyses of ZnO NRs were conducted using a field emission scanning electron microscope (FESEM; HITACHI S4800). The plasma-focused ion beam scanning electron microscope (PFIB-SEM, Helios 5 Hydra DualBeam, Thermo Scientific) was employed for the characterization of the cross-section structure of ZnO NRs. Before the PFIB-SEM characterization, ZnO NRs were spin-coated with AZ1505 photoresist (5000 rpm, 40 s) for sample protection. Length and diameter distribution of the ZnO NRs were measured from FESEM images using ImageJ software. The formation of the Ag/ZnO heterostructure was further confirmed by scanning transmission electron microscopy (STEM), selected area electron diffraction (SAED), and TEM energy-dispersive X-ray (TEM-EDX) analyses using a JEOL JEM-ARM200CF S/TEM with EDX (Narwhal). Diffuse reflectance spectra of ZnO NRs and Ag/ZnO NRs were acquired using a Hitachi U-3900H UV-visible spectrophotometer. Zn and Ag ion concentrations in the treated solutions were measured using inductively coupled plasma-optical emission spectroscopy (ICP-OES; Thermo iCAP6300 Duo).

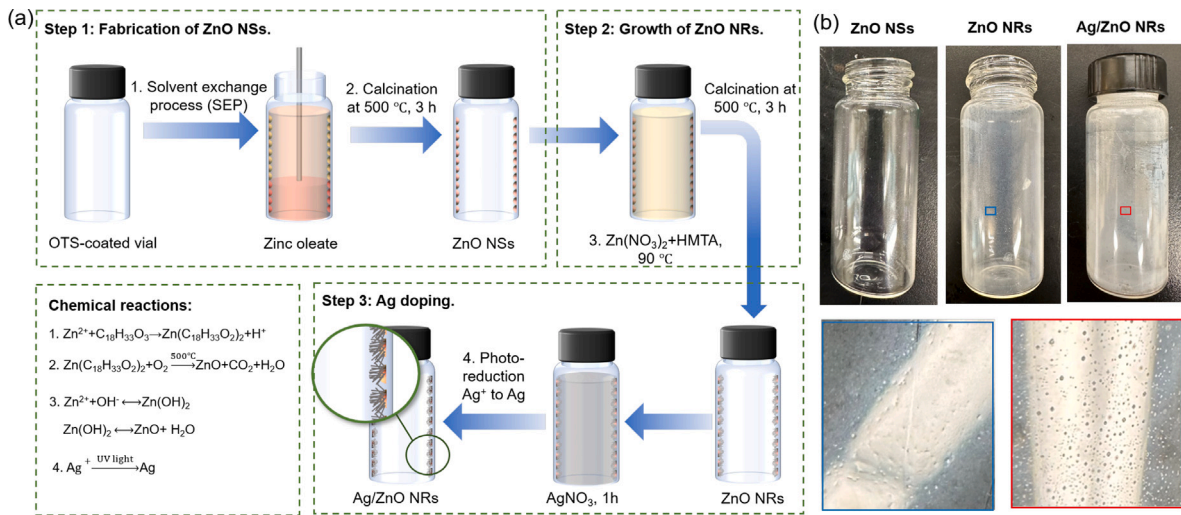


Fig. 1. (a) Steps in the fabrication of ZnO NSs, ZnO NRs, and Ag/ZnO NRs and the main chemical reactions involved. (b) Photos of vials coated with ZnO NSs, ZnO NRs, and Ag/ZnO.

2.5. Photocatalytic activity

Several parameters were investigated to evaluate the photocatalytic performance of the fabricated coated vials, including the oleic acid concentration in solution A during the SEP for ZnO NSs, the growth time of ZnO NRs, and the concentration of Ag in the fabrication of Ag/ZnO NRs. The photocatalytic activity was initially analyzed for the degradation of aqueous solutions containing SMX (5 mg/L) as a model organic contaminant under simulated solar light (SSL, SS200AAA Solar Simulation System, Photo Emission Tech) with a fixed irradiance of 112.53 W/m². Finally, the Ag/ZnO NRs-coated vial fabricated at the best synthesis conditions was applied under SSL for the treatment of a mixture containing eight MPs, including CAF, TMP, SMX, CBZ, ATZ, NPX, IPB, and GBZ, each at an initial concentration of 100 µg/L. The photodegradation efficiency (η) was calculated using Eq. (1):

$$\eta = \frac{C_0 - C_t}{C_0} \times 100\% \quad (1)$$

where C_0 and C_t are the initial concentration and the concentration at time t of each MP, respectively. To evaluate the stability of the Ag/ZnO NRs immobilized on the glass surface, four reuse experiments were performed to degrade the eight MPs in the matrix under the same reaction conditions. After each cycle, the Ag/ZnO NRs-coated vial was washed several times with deionized water and used in the next cycle of the photocatalytic treatment.

2.6. Analytical procedures

The evolution of SMX concentration during and after treatment with the coated vials was monitored using a UV–Vis spectrometer (Thermo Fisher Genesys 150). The concentrations of MPs in the mixture were analyzed using an Agilent 1290 Infinity II ultra-high-performance liquid chromatography (UHPLC) system coupled with an Agilent 6495 triple quadrupole mass spectrometer (LC-QQQMS, Agilent Technologies Inc.). Detailed information can be found in Text S1 in the supplementary information. Multiple reaction monitoring (MRM) transitions of the eight MPs are listed in Table S1. Before analysis, samples were collected and filtered through a 0.22 µm PTFE filter.

2.7. Reactive oxygen species (ROS) identification

ROS generated during the photocatalytic process were detected by electron spin resonance (ESR) measurements using a Bruker ELEXSYS-II E500 ESR spectrometer. ESR spectra were recorded with a magnetic

field modulation of 100 kHz, an amplitude of 1.0 G, microwave power of 20 mW, and a sweep time of 60 s. Samples were collected from the systems using a disposable microtube, sealed, and inserted into a 4 mm quartz ESR tube for analysis. •OH and •OH/O₂⁻ species were detected using DMPO (50 mM) and BMPO (200 mM) solutions as spin-trap reagents, respectively.

3. Results and discussion

3.1. Characterization of ZnO NRs and Ag/ZnO NRs

X-ray diffractograms were obtained for ZnO NRs and Ag/ZnO NRs samples, as shown in Figure S1. Both samples exhibit a well-crystallized and highly oriented hexagonal wurtzite ZnO structure, with a peak at a 2θ value of 34.4°, indexed as the (002) plane (JCPDS, File No. 036–1451) (Alharthi et al., 2020). In addition to the ZnO wurtzite structure, the Ag/ZnO NRs sample displays an additional peak at 38.1°, corresponding to the (111) plane of Ag nanoparticles (JCPDS, File No. 04–0783), confirming the formation of the Ag cubic structure on the ZnO NRs (Zamiri et al., 2014).

The morphology of the immobilized Ag/ZnO NRs was revealed by FESEM images, as shown in Figs. 2(a) and (b). ZnO was observed to grow in a rod-like structure with a rough surface and forming a circular pattern, while Ag nanoparticles were dispersed on the surface of ZnO NRs. FIB-SEM images of the cross-section of the Ag/ZnO NRs confirmed that this circular pattern consists of individual ZnO NRs (Fig. 2(c)), which exhibit a rough and porous surface (Fig. 2(d)). The size distribution of the internal pores in the Ag/ZnO NRs structure was analyzed using the ImageJ program, resulting in an average size of 23.93±6.67 nm (Figure S2). The NRs surface was also examined using STEM analyses, as shown in Figs. 2(e) to (g). Although smaller pores were observed, with an average size of 3.59±1.20 nm (Figure S3), the porous structure of the Ag/ZnO NRs is evident. This high surface area and large pore volume could enhance the photocatalytic performance of the immobilized material (Ahmad et al., 2021; Wu et al., 2021).

Moreover, as shown in 2(h), numerous spherical-like nanoparticles are visible on the surface of the ZnO NRs, contributing to the overall surface morphology. Fig. 2(i) presents a magnified image of one of these like-spherical nanoparticles, where well-defined lattice fringes indicate its crystalline nature. The lattice fringe with an interplanar spacing of 0.24 nm corresponds to the (111) plane of Ag, indicating the successful deposition of Ag nanoparticles into the ZnO NRs structure. The SAED pattern of the Ag/ZnO (Fig. 2(j)) also indicates a high crystallinity of the sample, with the spot indexing confirming

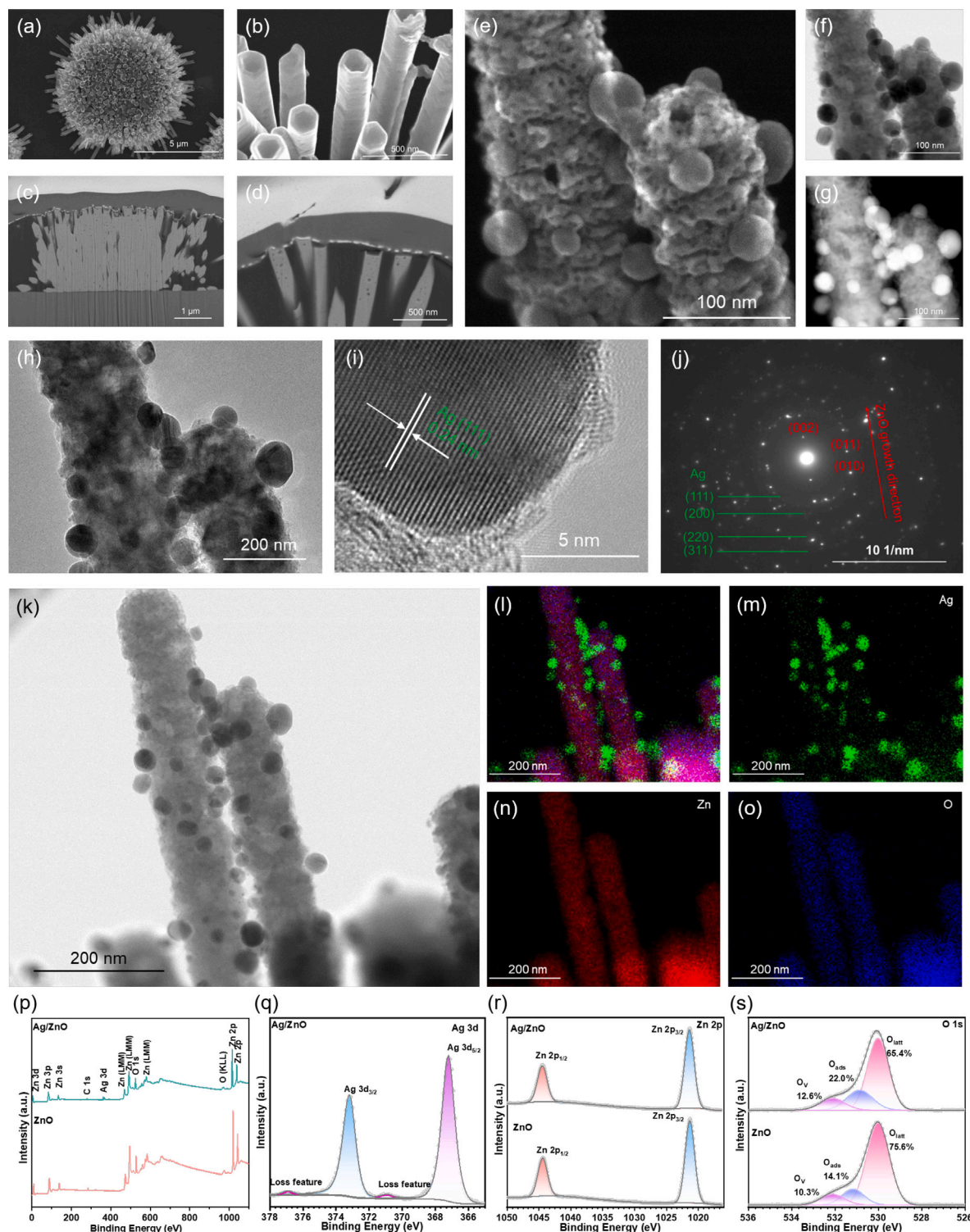


Fig. 2. Characterizations: FESEM images with (a) low and (b) high magnification. PFIB-SEM images of the cross-section pattern with (c) low and (d) high magnification. (e) STEM image and STEM images with (f) high-angle annular dark-field (HAADF-STEM) and (g) high-angle annular bright-field (HAABF-STEM). High-resolution TEM images with (h) low and (i) high magnification. (j) SAED pattern. TEM-EDX analyses from (k) to (o). (p) XPS survey scan spectrum and XPS scan spectra of (q) Ag 3d, (r) Zn 2p, and (s) O 1s for ZnO NRs and Ag/ZnO NRs.

the wurtzite structure of ZnO, as discussed in the XRD results above. Furthermore, EDX analysis was carried out further to confirm the elemental composition of the material. According to the EDX elemental mapping images shown in Figs. 2(k) to (o), rod-like structures are predominantly composed of Zn (in red) and O (in blue) elements, while Ag (in green) nanoparticles are distributed along the NRs surface, confirming their successful incorporation in the photocatalyst.

To demonstrate the impact of Ag deposition on the surface chemical state of ZnO NRs, a detailed XPS analysis of ZnO NRs and Ag/ZnO NRs samples was conducted. The corresponding survey XPS spectra, along with high-resolution Ag 3d, Zn 2p, and O 1s XPS spectra, are shown in Fig. 2(p)–(s). The binding energies in the XPS spectra were calibrated using C 1s (284.8 eV). Strong signals from Zn, O, Ag, and C elements are observed in the Ag/ZnO survey spectra (Fig. 2(p)), indicating the high purity of the Ag/ZnO photocatalyst. Fig. 2(q) presents the high-resolution Ag 3d XPS spectra of Ag/ZnO NRs, where two peaks at 367.20 and 373.20 eV correspond to Ag 3d_{5/2} and Ag 3d_{3/2}, respectively. The splitting of the 3d doublet is approximately 6.0 eV, indicating the metallic nature of Ag (Chen et al., 2024). Symmetrical peaks in Fig. 2(r) at 1021.32 and 1044.54 eV for ZnO and Ag/ZnO NRs samples correspond to Zn 2p_{3/2} and Zn 2p_{1/2}, respectively. The splitting of Zn-2p states was about 23 eV, confirming the presence of Zn²⁺ lattice ions (Mou et al., 2018; Chen et al., 2024). Fig. 2(s) illustrates the oxygen levels (O) in both samples. The O 1s curve is asymmetric and was fitted with three Gaussian peaks. The peaks located at approximately 530.01 eV, 531.17 eV, and 532.12 eV in both ZnO and Ag/ZnO samples are attributed to lattice oxygen (O_{latt}), adsorbed oxygen (O_{ads}), and oxygen vacancies (O_v) (Mahrsi et al., 2023). Quantitative XPS analysis shows that the percentage of O_{latt} and O_v in Ag/ZnO increased from 14.1% and 10.3% to 22.0% and 12.6%, respectively, indicating that the concentration of oxygen vacancies and surface hydroxyl oxygen in Ag/ZnO NRs is higher than in ZnO NRs. Oxygen vacancies and surface hydroxyl oxygen play crucial roles in semiconductor photocatalysis and enhance photocatalytic activity (Li et al., 2022b). Therefore, the photocatalytic activity of ZnO NRs should increase following the Ag deposition process.

3.2. Effect of oleic acid concentration on the fabrication of ZnO NSs

ZnO NSs were pre-immobilized inside OTS glass vials using a SEP, as illustrated in step 1 of Fig. 1(a). During this process, the oversaturation of oleic acid in the mixture leads to the formation of oleic acid droplets on the inner surface of the vial, which serve as a pattern for forming zinc oleate nanoparticles and ZnO NSs after calcination. In this sense, adjusting the concentration of oleic acid in solution A during SEP can influence the average size of the droplets and the surface coverage on the substrate, potentially affecting the growth of ZnO NRs in step 2 and the photocatalytic performance of the system (Lu et al., 2024).

To investigate this parameter, different concentrations of oleic acid (ranging from 1% to 4% V/V) in solution A were tested, and the size distribution and surface coverage rate of ZnO NSs were analyzed. The photocatalytic performance of ZnO NRs grown on ZnO NSs was also evaluated for SMX degradation under SLL. Figs. 3(a) and (c) display representative photos of ZnO NSs-coated vials and ZnO NRs-coated vials at various oleic acid concentrations, respectively. ZnO NSs were immobilized across the inner surface of the vials, which remained almost transparent after the process, especially for oleic acid concentrations of 1% and 2%. The transmittance of each coated vial is shown in Figure S4. Optical microscopic images were captured at the top, middle, and bottom positions of each vial to evaluate the size distribution of ZnO NSs along the vertical axis, as shown in Fig. 3(b). The particle size of ZnO NSs increased with higher concentrations of oleic acid, resulting in a wider size distribution. Lower levels of oleic acid (i.e., 1% and 2%) resulted in a more homogeneous and uniform distribution of ZnO NSs, while higher concentrations led to the formation of larger ZnO NSs and a more heterogeneous size distribution.

The effect of fabrication conditions on the surface coverage rate and the average size of ZnO NSs was analyzed using ImageJ software, as shown in Figs. 3(d) and (e), respectively. A maximum surface coverage rate of 34.5% was achieved with 2% oleic acid, while a minimum rate of 18.3% was observed with 1%. Intermediate coverage rates of 28.9% and 26.4% were observed with 3% and 4% oleic acid, respectively. In addition, the average diameter of ZnO NSs showed a clear trend to increase with the oleic acid concentration, ranging from 3.4 μm to 11.6 μm for concentrations from 1% to 4%. Moreover, the photodegradation efficiency of ZnO NRs grown on ZnO NSs fabricated with different oleic acid concentrations was evaluated for SMX degradation. Fig. 3(f) shows that all conditions demonstrated effective degradation performance after 10 h of exposure to SSL, with photodegradation efficiencies of over 90.0%. However, the ZnO NR-coated vial fabricated with 2% oleic acid achieved a degradation percentage of 97.1%, compared to 90.0% at the highest oleic acid concentration of 4%. Interestingly, 1% oleic acid, which resulted in the lowest coverage rate and average diameter, exhibited better photodegradation performance (94.0%) than 4%. This suggests that coverage rate and average diameter are not the only factors influencing the photocatalytic performance of ZnO NRs.

As shown in Fig. 4(a), FESEM images of ZnO NRs with varying pattern sizes were captured to analyze the ZnO NRs structure in detail. When the pattern size of ZnO NRs is 2.1 μm, the NRs grow randomly and interlace with each other. At a pattern size of 3.0 μm, ZnO NRs continue to grow randomly, interlacing primarily at the edges. However, at pattern sizes over 5.0 μm, the NRs exhibit an ordered alignment trend in the central area. This phenomenon is more clearly observed in FIB-SEM images of the cross-section of each ZnO NRs pattern, as shown in Fig. 4(b). It is evident that NRs grow independently when the bottom seed size is around 2.0 μm but become organized and densely packed in the central area at larger sizes. Additionally, top-view and cross-sectional images of ZnO NRs show that the thickness remains at 1.0 μm, indicating that ZnO NRs begin to grow densely in the central area at seed sizes larger than 2.0 μm. This dense growth may reduce the active surface area of the photocatalyst, thereby decreasing its performance in degrading SMX. To quantify this effect, the total active surface area (TASA) of each ZnO NR pattern was calculated considering the central and edge areas, as illustrated in Fig. 4(c), and using the equations below.

$$TASA_{pattern} = N_{NRs} \cdot ASA_{NR} \quad (2)$$

$$N_{NRs} = A_{pattern} / CA_{NR} \quad (3)$$

$$ASA_{NR} = \pi \cdot (D_{NR}/2)^2 + CA_{NR} \quad (4)$$

Here, N_{NRs} is the number of NRs in one pattern, ASA_{NR} is the active surface area of a single NR, $A_{pattern}$ is the total area of the pattern, CA_{NR} is the contact area of one NR with ZnO NS, and D_{NR} is the diameter of a single NR. When the seed size is less than 2.0 μm, each ZnO NR has 100% active surface area (ASA). At seed sizes larger than 2.0 μm, ZnO NRs at the 1.0 μm edge still have 100% ASA, but in the central area, due to the dense growth, only the top 20% of the area is in contact with contaminants. Therefore, TASA was calculated as follows:

$$TASA_{pattern} = TASA_{edge} + TASA_{center} \quad (5)$$

$$TASA_{edge} = N_{edgeNRs} \cdot ASA_{NR} \quad (6)$$

$$TASA_{center} = N_{centerNRs} \cdot ASA_{NR} \cdot 20\% \quad (7)$$

Where $TASA_{edge}$ and $TASA_{center}$ are the total active surface area of NRs at the edge and center areas of each pattern, respectively. $N_{edgeNRs}$ and $N_{centerNRs}$ are the number of NRs at the edge and center areas of each NRs pattern, respectively. The calculated TASA per unit area of each ZnO NR pattern is shown in Fig. 4(f), assuming a surface coverage rate of 30% (average of surface coverage rates in Fig. 3(d)). The TASA per unit area is constant at 5.75 m²/m² for seed sizes less than

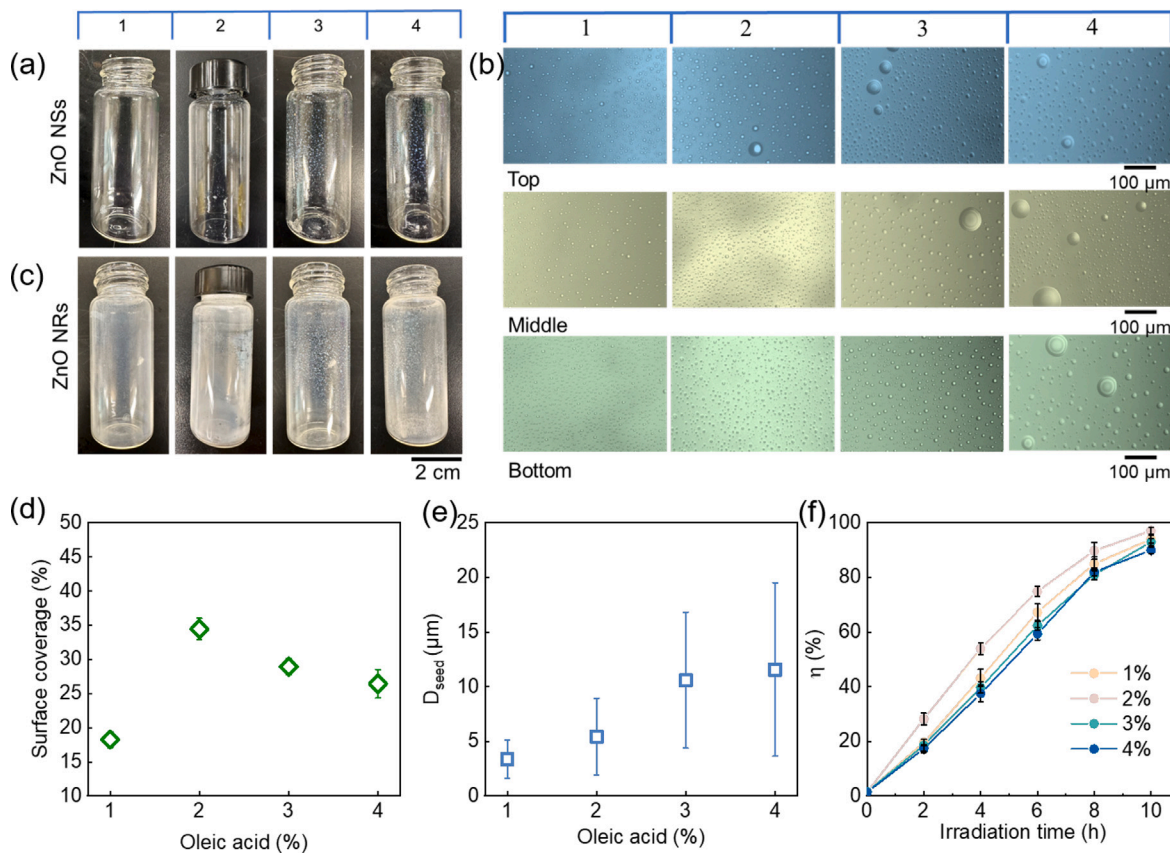


Fig. 3. (a) Photos of ZnO NSs-coated vials, (b) optical microscopic images of ZnO NSs on vials, (c) photos of ZnO NRs-coated vials, (d) surface coverage rates of ZnO NSs on vials, (e) average diameter of ZnO NSs on vials, and (f) photodegradation efficiency of SMX with ZnO NRs growth on the ZnO NSs under simulated solar light.

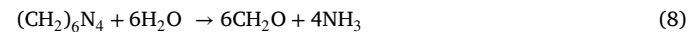
2.0 μm but decreases when seed size exceeds 2.0 μm . Thus, lower oleic acid concentrations in solution A during the SEP are more suitable for obtaining smaller ZnO NR patterns that result in higher TASA values.

However, adjusting the oleic acid concentration also affects the surface coverage rate of ZnO NR patterns (Fig. 4(d)), which is another crucial parameter for TASA calculation. Fig. 4(g) shows the TASA of ZnO NRs calculated using the analyzed average size and surface coverage rate of ZnO NR patterns fabricated at different oleic acid concentrations. The calculated results show the order: TASA(2%) > TASA(1%) > TASA(3%) > TASA(4%), which correlates well with the photodegradation performance observed in Fig. 3(g). Notably, a larger surface coverage rate does not always imply better photodegradation efficiency, as the growth mechanism of the nanoparticles affects their active photocatalytic area (Kusiak-Nejman et al., 2021).

3.3. Influence of growth time on the morphology of ZnO NRs

Growth time is an important experimental parameter that influences the morphology of ZnO NRs (Khan et al., 2020; Zhang et al., 2020b). Figs. 5(a) and (b) show side and top views, respectively, of FESEM images of ZnO NRs grown for different times (from 2 to 10 h). The statistical average length (Fig. 5(c)) and average diameter (Fig. 5(d)) of individual ZnO NRs were determined by randomly measuring the captured FESEM images of the side and top views, respectively. It was observed that growth time had a slight influence on the average length, increasing from $0.89 \pm 0.09 \mu\text{m}$ at 2 h to $0.97 \pm 0.024 \mu\text{m}$ at 10 h. However, a significant increase in the average diameter was noted, ranging from $0.11 \pm 0.03 \mu\text{m}$ to $0.31 \pm 0.09 \mu\text{m}$ over the same period. This indicates that lateral growth was favored over axial growth as the time increased from 2 to 10 h, a behavior also reported in other studies (Shabannia, 2016).

In this study, as shown in Fig. 1(a), ZnO NRs were grown on a preseeded substrate by mixing solutions of $\text{Zn}(\text{NO}_3)_2$ and HMTA (0.04 M each) in a 1:1 volume ratio at 90 °C using a hydrothermal synthesis method. ZnO crystals have polar faces ((001) and (002)) with higher surface energy than non-polar faces ((100) and (101)) (Tan et al., 2021). These polar faces are metastable and more likely to participate in chemical reactions to decrease the free energy of the system (such as during hydrothermal growth and etching effect) (Tan et al., 2021; Montero-Muñoz et al., 2020). Typically, during the growth process of bulk ZnO NRs, OH^- ions supplied by HMTA (chemical Eqs. (8) and (9)) settle on the oppositely charged (001) face and react with Zn^{2+} ions to form $\text{Zn}(\text{OH})_2$ (Eq. (10)), promoting growth along the (001) direction. Finally, $\text{Zn}(\text{OH})_2$ decomposes into ZnO (Gerbrelders et al., 2020; Tan et al., 2021), as can be seen in Eq. (11). In our approach, the highly oriented ZnO NRs selectively grew on the (002) plane, as discussed in the XRD patterns in Figure S1. This preferred orientation in the (002) direction is consistent with previous reports (Cerrón-Calle et al., 2019; Young et al., 2021; Zheng et al., 2020).



The ZnO NR growth process can be divided into two stages based on growth time. The first stage begins with a high OH^- concentration produced during the hydrolysis of HMTA $((\text{CH}_2)_6\text{N}_4)$. In this stage, the dissolution-secondary precipitation process is dominant, resulting in the formation of uniform and long ZnO NRs. As the growth time increases, the OH^- concentration and the amount of Zn^{2+} ions decrease

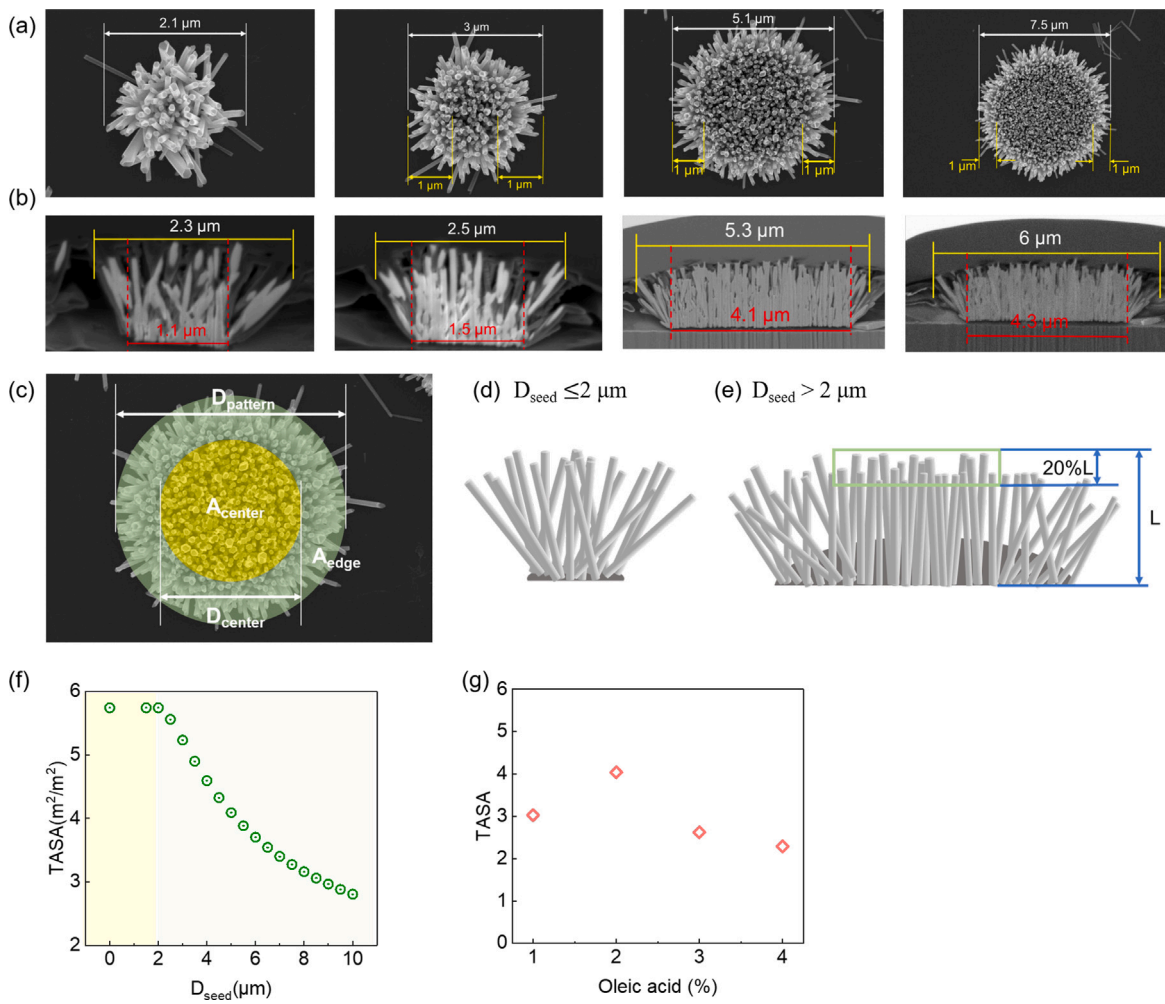


Fig. 4. (a) FESEM images of the top view of ZnO NR patterns with different pattern sizes. (b) FIB-SEM images of the cross-sections of each ZnO NR pattern. (c) Sketch of ZnO NR patterns showing the division of central and edge regions. (d) Sketch of ZnO NR patterns with $D_{seed} \leq 2 \mu\text{m}$. (e) Sketch of ZnO NR patterns with $D_{seed} > 2 \mu\text{m}$. (f) Calculated TASA for each ZnO NR pattern, assuming a surface coverage rate of 30%. (g) Calculated TASA of ZnO NRs as a function of the oleic acid concentrations in solution A.

significantly, leading to slower growth on both the polar and non-polar faces. Meanwhile, an etching process occurs on the polar face, reducing the length of the ZnO NRs after a prolonged growth period (Gerbreders et al., 2020). Thus, longer growth times result in a slight increase in the length of ZnO NRs while significantly increasing their diameter. This dual effect influences the TASA in two opposing ways: the increase in average length enhances the TASA due to the larger surface area, while the increase in diameter can reduce the overall efficiency of light absorption due to decreased space between the ZnO NRs. Consequently, TASA is affected both positively and negatively by changes in the dimensions of the ZnO NRs with varying growth times.

To determine the optimal growth time of ZnO NRs for achieving the best photocatalytic performance, SMX photodegradation experiments were conducted using ZnO NRs-coated vials fabricated with different growth times. As shown in Fig. 5(e), the ZnO NRs-coated vial with a growth time of 6 h exhibited the highest photodegradation efficiency, followed by those grown for 4 h. As expected, the longest growth time (10 h) resulted in the lowest photodegradation efficiency. These results further confirm the dual effect of growth time on the photocatalytic performance of ZnO NRs.

3.4. Effect of Ag deposition on the photocatalytic activity of ZnO NRs

Depositing Ag nanoparticles into ZnO has been proven to enhance photocatalytic activity by narrowing the band gap energy and improving charge carrier separation efficiency (Ahmad et al., 2022). Additionally, Ag/ZnO exhibits better stability against photo-corrosion than pure ZnO (Singh, 2022). In our study, Ag nanoparticles were coated onto the surface of ZnO NRs via the photo-reduction of Ag^+ by UV light, as represented in Fig. 2. Ag/ZnO NRs-coated vials with different Ag deposition content were used to degrade SMX aqueous solutions (5 mg/L) under 10 h of exposure to SSL, as shown in Fig. 6(a). Experiments under dark conditions (adsorption) and using only SSL (photolysis) were conducted as a control, and negligible degradation rates were observed. In contrast, a 97% photodegradation efficiency was achieved using the ZnO NRs-coated vial. Despite this excellent performance, depositing Ag into the ZnO NRs structure further improves photodegradation rates, reaching almost 100% efficiency in only 4 h for vials fabricated from 0.05 M to 0.1 M of AgNO_3 . This positive effect on degradation kinetics is also noticeable for 0.01 M and 0.03 M AgNO_3 , although to a lesser extent.

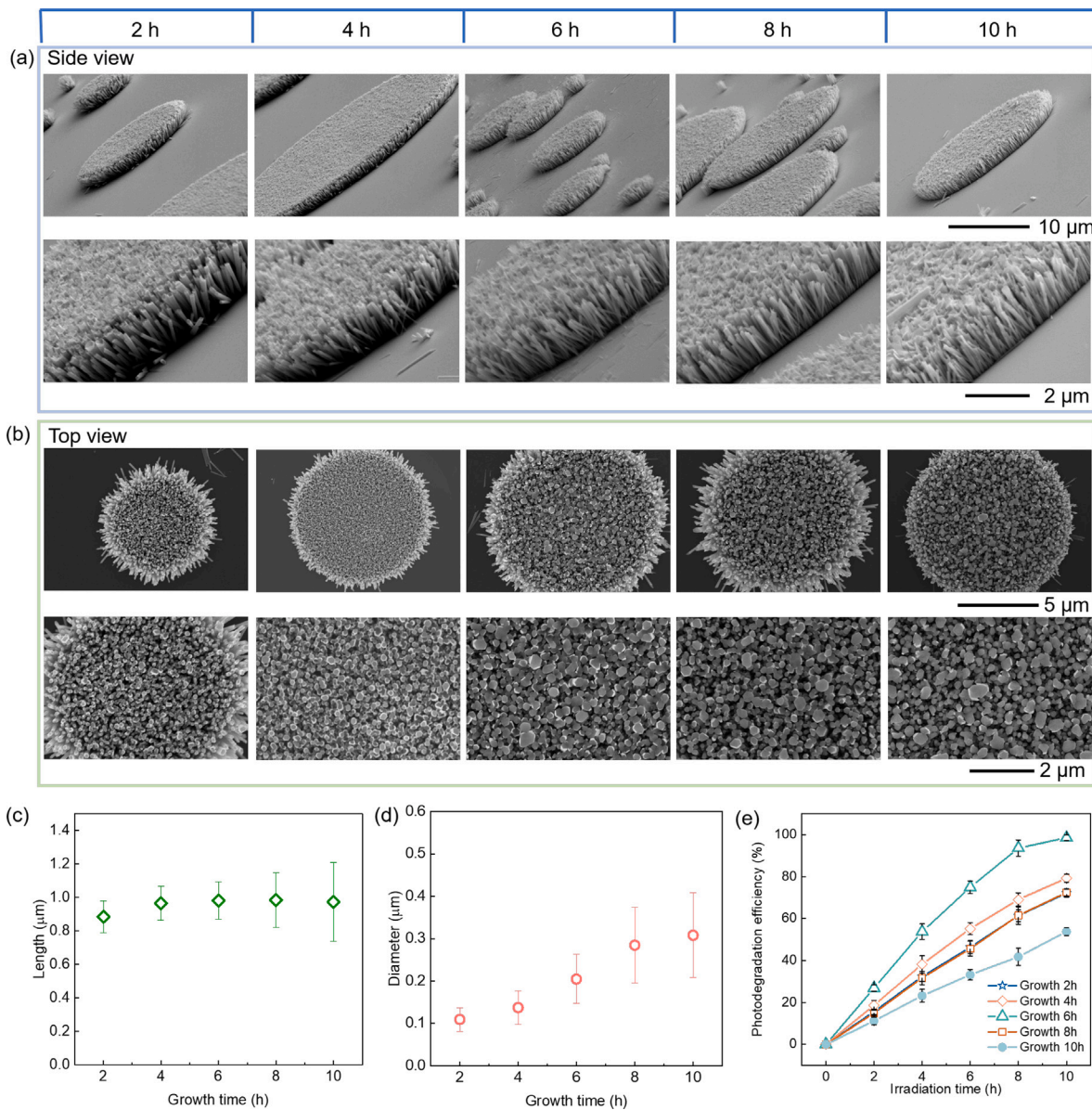


Fig. 5. FESEM images of (a) side view and (b) top view of ZnO NRs with different growth time. (c) Average length and (d) average diameter of single ZnO NR with different growth time, and (e) photodegradation efficiency of SMX with ZnO NRs-coated vials fabricated with different growth times.

Moreover, a kinetic analysis for the photodegradation of SMX by ZnO NRs and Ag/ZnO NRs under SSL was conducted using Eq. (12).

$$\ln\left(\frac{C_0}{C_t}\right) = kt \quad (12)$$

Where C_0 and C_t represent the concentration of SMX at time 0 h and at time t , respectively, and k represents the pseudo-first-order kinetic constant (h^{-1}). Table S2 summarizes the pseudo-first-order kinetic constants obtained with their corresponding R^2 . From Figure S5, it is clear that k values increase when increasing the concentration of AgNO_3 in the fabrication process, reaching the highest value at 0.05 M. Additionally, the enhancement factor of ZnO NRs with Ag was calculated according to Eq. (13), with $k_{\text{Ag}/\text{ZnO}}$ and k_{ZnO} being the pseudo-first-order kinetic constants for the Ag/ZnO NRs and ZnO NRs systems, respectively.

$$\text{Enhancement factor} = \frac{k_{\text{Ag}/\text{ZnO}}}{k_{\text{ZnO}}} \quad (13)$$

As shown in Fig. 6(b), Ag deposition has a significant enhancement on the photodegradation performance of ZnO NRs. The enhancement

factor reached the maximum value at 2.9 when increasing the AgNO_3 concentration from 0.01 M to 0.05 M. In this sense, 0.05 M was selected as the best Ag^+ precursor concentration to investigate the photocatalytic activity of the Ag/ZnO NRs in the following analyses.

To further investigate the enhancement effect of Ag deposition on the photodegradation performance of ZnO NRs, the UV-Vis diffuse reflectance spectra of ZnO NRs and Ag/ZnO NRs (0.05 M Ag precursor) samples were measured, as shown in Figure S6. The E_g of these samples was calculated based on the diffuse reflectance spectra using Tauc's equation (López and Gómez, 2012).

$$(F(R)hv)^{1/2} = B(hv - E_g) \quad (14)$$

Where $F(R)$ is the Kubelka-Munk function, h is the Planck constant, ν is the photon's frequency, E_g is the band gap energy, and B is a constant. The E_g of ZnO NRs was observed to be 3.20 eV, while a slight decrease to 3.18 eV was observed after the deposition of Ag (Figs. 6(c) and (d)). As previously reported, incorporating Ag nanoparticles into ZnO generates oxygen vacancies, thereby reducing the E_g and enhancing the efficiency of visible light absorption (Singh, 2022). Moreover,

ESR spectra were recorded to compare the main ROS generated using both materials under SSL. $\cdot\text{OH}$ and $\cdot\text{O}_2^-$ have been reported as the dominant radicals in ZnO-based photocatalytic systems (Liu et al., 2020; Shen et al., 2022; Feng et al., 2020). DMPO was used as a trapping agent to detect the generation of $\cdot\text{OH}$ species during the ESR analysis. Fig. 6(e) shows that no signals of the adduct DMPO- $\cdot\text{OH}$ were observed in the blank experiment, conducted using only SSL for 15 min. In contrast, typical DMPO- $\cdot\text{OH}$ signals were detected after the illumination of both ZnO NRs and Ag/ZnO NRs-coated vials with SSL, indicating the generation of $\cdot\text{OH}$ species in both systems. Notably, the intensity of the DMPO- $\cdot\text{OH}$ peaks in the Ag/ZnO NRs system was higher (around 1.60 times) than in the ZnO NRs, as shown in Figure S7. Additionally, the possible generation of $\cdot\text{O}_2^-$ was investigated using BMPO as a trapping agent. Results in Fig. 6(f) show that signals for the BMPO- $\cdot\text{O}_2^-$ adduct were observed in both ZnO NRs and Ag/ZnO NRs systems. Similarly, the intensity of the BMPO- $\cdot\text{O}_2^-$ signals was higher in the Ag/ZnO NRs vial, indicating that Ag successfully increased the generation of ROS, further enhancing the photocatalytic activity of ZnO NRs.

Based on the discussion above, the photocatalytic mechanism of Ag/ZnO NRs is proposed in Figure S8. When ZnO NRs are exposed to the SSL, electrons in the valence band (VB) are excited to the conduction band (CB), generating electron-hole pairs. The photogenerated electrons in the CB transfer to Ag particles because the CB energy level of ZnO is higher than the Fermi level of metallic Ag (Rabell et al., 2021). As a result, the separation efficiency and the lifetime of the photogenerated e^-/h^+ pairs are improved. The generated h^+ in the VB of ZnO oxidize water and hydroxyl groups to form $\cdot\text{OH}$, while the photogenerated e^- react with oxygen to form $\cdot\text{O}_2^-$ species (Zhang et al., 2020a; Qi et al., 2021). These $\cdot\text{OH}$ and $\cdot\text{O}_2^-$ species, along with the holes are responsible for effectively degrading the target contaminant (Shang et al., 2023).

Finally, the SMX degradation efficiency using immobilized Ag/ZnO NRs in the best fabrication conditions (2% of oleic acid concentration during SEP, 6 h of hydrothermal growth time, and 0.05 M of AgNO_3 precursor) were compared with those of other dispersed and immobilized ZnO-based photocatalysts reported in the literature (Table S3). This immobilized Ag/ZnO NRs exhibit similar photodegradation performance for SMX degradation as dispersed ZnO-based photocatalysts, albeit with a longer irradiation time (Akbari et al., 2023; Makropoulou et al., 2020; Dhiman et al., 2021; Mirzaei et al., 2018a; Roy et al., 2023). Furthermore, the current photocatalyst exhibited a 5-fold higher photodegradation efficiency compared to immobilized ZnO nanocaps (Li et al., 2023).

3.5. Application in the photodegradation of a mixture of MPs

A solution containing eight MPs, including CAF, TMP, SMX, CBZ, ATZ, NPX, IBP, and GBZ (see chemical structures in Table S4), with a total initial concentration of 800 $\mu\text{g/L}$ (100 $\mu\text{g/L}$ each MP), was used to further investigate the performance of ZnO NRs and Ag/ZnO NRs-coated vials. These contaminants were selected due to their frequent detection in natural water and wastewater, typically at concentrations ranging from ng/L to $\mu\text{g/L}$ (Fekadu et al., 2019; Adeleye et al., 2022; de Albuquerque et al., 2020).

Before the photocatalysis degradation of the mixture of MPs, control experiments using only SSL were performed. As can be seen in Figure S9, no important photodegradation was observed for all the MPs (except NPX with 38.0% photodegradation) in 6 h of exposure to only SSL, whereas photodegradation percentages close to 100% were achieved when using the ZnO NRs-coated vial under the same irradiation time (Fig. 7(a)). ATZ shows slower photodegradation kinetics than the other MPs but reaches 92.0% degradation after treatment. Remarkably, Ag/ZnO NRs-coated vial under SSL led to almost complete photodegradation of all eight MPs (including ATZ) within just 4 h, as shown in Fig. 7(b). The total photodegradation efficiency in this system,

i.e., considering the eight MPs, was calculated and shown in Figure S10. Photodegradation kinetics analyses conducted for the eight MPs in the ZnO NRs and Ag/ZnO NRs systems, showed in Figs. 7(c) and (d), respectively, confirm the superior performance of the Ag/ZnO NRs-coated vial. Table S5 presents the pseudo-first-order kinetic constants with their corresponding R^2 values. Furthermore, Fig. 7(e) presents the enhancement factors for the Ag-coated material. A 3.06-fold enhancement factor was obtained for ATZ, while enhancement factors between 1.33- and 2.15-fold were obtained for the other 7 MPs compared to those in the ZnO NRs-coated vial.

To evaluate the stability of the immobilized material on the glass container, the Ag/ZnO NRs-coated vial was reused in four consecutive cycles of photodegradation experiments. Solutions containing the eight MPs were used as the working matrix, with a fixed irradiation time of 6 h for each cycle. As shown in Fig. 7(f), even after four reuse cycles, the photodegradation efficiency of the Ag/ZnO NRs-coated vial for the total degradation of MPs remained close to 100%. This suggests that the catalyst is stable to photocorrosion and minimal metal leaching occurred. This latter was confirmed by ICP-OES, quantifying the Zn and Ag content in the solution after a long-term experiment (24 h). The concentration of Zn in solution was below the limit of detection ($\text{LoD} = 0.004 \text{ mg/L}$) of the instrument, indicating less or no Zn leached from the Ag/ZnO NRs. For comparison, the concentration of Zn measured in the solution after using the ZnO NRs-coated vial was 0.021 mg/L (at least 5 times higher), suggesting that the deposition of Ag on the surface of the ZnO NRs significantly improves the material stabilization. Previous studies have shown that loading small amounts of Ag onto ZnO can suppress photocorrosion by facilitating the rapid transfer of photoexcited electrons from ZnO to Ag nanoparticles, thereby increasing the e^-/h^+ pair lifetime and enhancing h^+ utilization in the degradation process (Muñoz-Fernandez et al., 2022; Chankhanitha et al., 2021; Ma et al., 2017). Furthermore, only 0.003 mg/L of Ag was detected after the long-term experiment, which is below both the US EPA Secondary Maximum Contaminant Level and the WHO recommended level of 0.1 mg/L for Ag in drinking water. The excellent stabilization of the photocatalyst on the glass surface may also be associated to the *in-situ* fabrication of NSs during the SEP. Previous work demonstrated that immobilized metal oxide NSs on a silicon substrate exhibited good stability, even after 60 min under ultrasonication (Wei et al., 2022). In our study, the contact between the ZnO NSs and the glass surface during the *in-situ* formation process is governed by van der Waals forces, resulting in strong adhesion between the NSs and the vial surface, enhancing the immobilization of the resulted ZnO NRs after the calcination process.

4. Conclusions

Porous ZnO NRs and Ag/ZnO NRs photocatalysts were successfully immobilized on the inner surface of a glass vial for the first time using a novel SEP followed by a hydrothermal method. Based on the results of this study, the following conclusions can be drawn:

- The maximum active surface area of ZnO NRs, with the best photocatalytic performance, was achieved by tuning the oleic acid concentration (2.0%) and hydrothermal growth time (6 h).
- Depositing Ag nanoparticles onto ZnO reduced the E_g from 3.20 eV to 3.18 eV, enhancing the photocatalytic activity by 2.9-fold.
- The application of Ag/ZnO NRs for the photodegradation of a mixture of eight MPs at relevant environmental concentrations demonstrated remarkable performance, achieving over 99% total degradation of MPs across several consecutive reuse cycles.
- Ag/ZnO NRs exhibit excellent photo-stability, remaining stable even after a long-term experiment lasting 24 h, with minimal metal leaching into the treated solutions and meeting the recommended levels for drinking water.

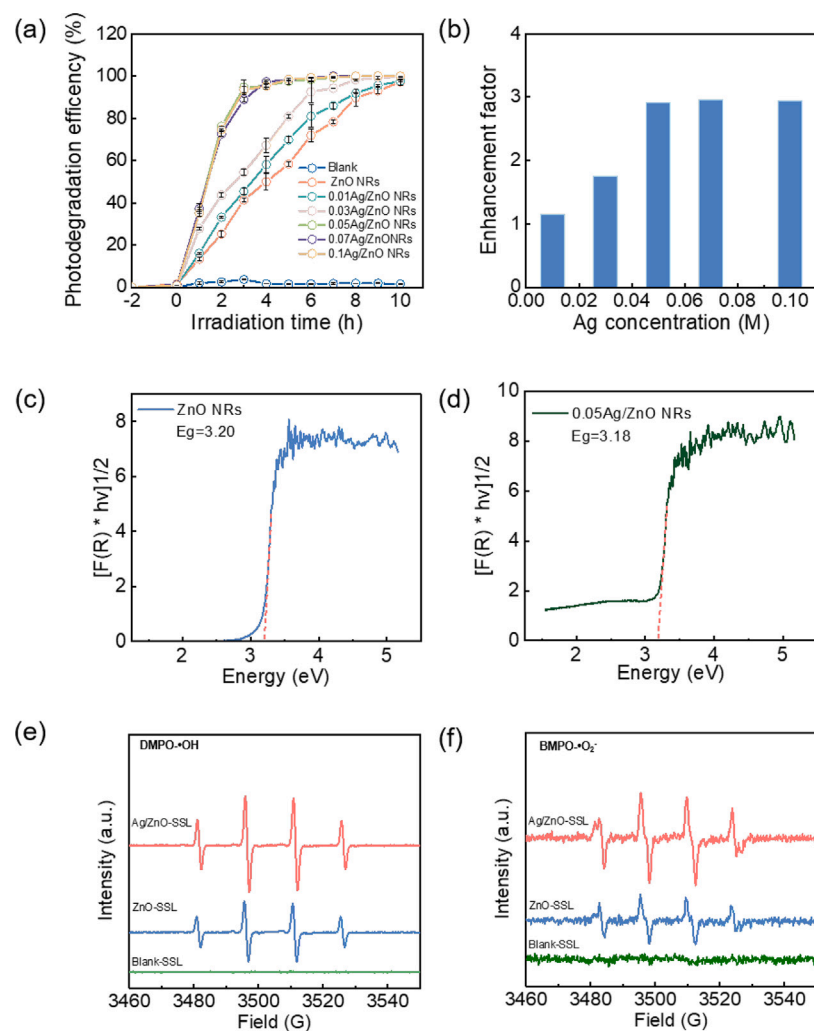


Fig. 6. (a) Photodegradation efficiency of SMX by SSL (blank), ZnO NRs, and Ag/ZnO NRs with different concentrations of Ag precursor. (b) Photodegradation enhancement factor for SMX degradation using Ag/ZnO NRs with different concentrations of Ag precursor. Kubelka-Munck plots for (c) ZnO NRs and (d) 0.05 Ag/ZnO NRs. ESR spectrum of (e) DMPO·OH in both ZnO NRs and Ag/ZnO NRs system and (f) ESR spectrum of BMPO·O₂[−] in ZnO NRs and Ag/ZnO NRs system. All experiments were conducted under SSL.

Therefore, this novel approach for the immobilization of photocatalyst on the glass substrate presents a promising solution to the recovery and reuse challenges commonly encountered in the photocatalytic treatment of water by semiconductors photocatalysts.

CRediT authorship contribution statement

Yanan Li: Writing – original draft, Visualization, Investigation, Formal analysis, Data curation, Conceptualization. **Isaac Sánchez-Montes:** Writing – review & editing, Investigation, Formal analysis, Data curation. **Lingling Yang:** Formal analysis. **Mohamed Gamal El-Din:** Writing – review & editing, Supervision, Resources, Funding acquisition, Conceptualization. **Xuehua Zhang:** Writing – review & editing, Supervision, Resources, Funding acquisition, Conceptualization.

Declaration of competing interest

The authors declare that they have no known competing financial interests or personal relationships that could have appeared to influence the work reported in this paper.

Acknowledgments

This research has been funded by the Natural Sciences and Engineering Research Council of Canada (NSERC) Senior Industrial Research

Chair (IRC) in Oil Sands Tailings Water Treatment with the support of Canada's Oil Sands Innovation Alliance (COSIA), Suncor Energy Inc., Canada, Syncrude Canada Ltd., Imperial Oil Resources, Teck Resources Limited, Canadian Natural Resources Ltd., EPCOR Water Services, Alberta Innovates, Canada, and Alberta Environment and Parks, Canada. We also acknowledge the Canada Research Chairs Program and NSERC Discovery Grants Program for their contributions to our research. This study, which is part of the University of Alberta's Future Energy Systems (FES) research initiative, also appreciated the funding from the Canada First Research Excellence Fund. Yanan Li acknowledges the financial support from the China Scholarship Council, China. Technical support from nanoFAB at the University of Alberta is also gratefully acknowledged.

Appendix A. Supplementary materials

Supplementary material related to this article can be found online at <https://doi.org/10.1016/j.watres.2024.122736>.

Data availability

No data was used for the research described in the article.

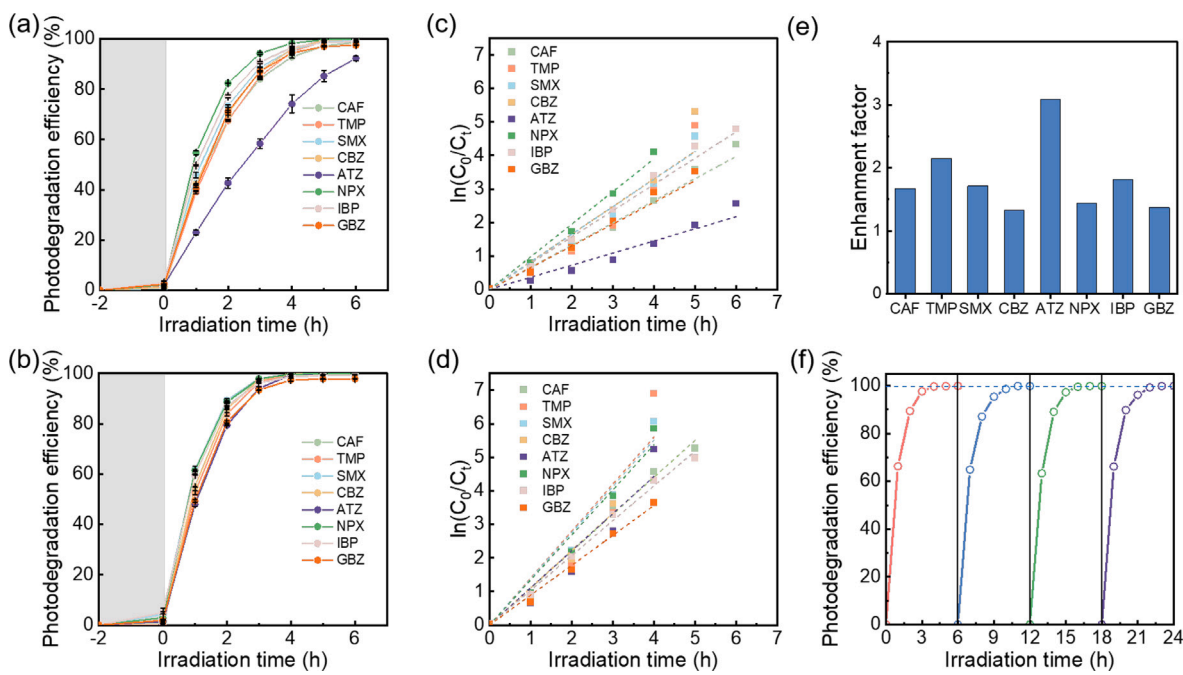


Fig. 7. Photodegradation efficiency of eight MPs, (a) with ZnO NRs, and (b) with 0.05 Ag/ZnO NRs. Photodegradation kinetics of eight MPs, (c) with ZnO NRs, and (d) with 0.05 Ag/ZnO NRs. (e) Photodegradation enhancement factor of eight MPs with 0.05 Ag/ZnO NRs. (f) Photodegradation efficiency of eight MPs with 4 cycles reuse of 0.05 Ag/ZnO NRs-coated vial. All experiments were conducted under the irradiation of SSL.

References

- Adeleye, Adeyemi S., Xue, Jie, Zhao, Yixin, Taylor, Alicia A., Zenobio, Jenny E., Sun, Yian, Han, Ziwei, Salawu, Omobayo A., Zhu, Yurong, 2022. Abundance, fate, and effects of pharmaceuticals and personal care products in aquatic environments. *J. Hazard. Mater.* 424, 127284.
- Ahamad, Tansir, Naushad, Mu, Alshehri, Saad M., 2021. Analysis of degradation pathways and intermediates products for ciprofloxacin using a highly porous photocatalyst. *Chem. Eng. J.* 417, 127969.
- Ahmad, Irshad, Akhtar, Muhammad Shoaib, Ahmed, Ejaz, Ahmad, Mukhtar, 2020. Highly efficient visible light driven photocatalytic activity of graphene and CNTs based Mg doped ZnO photocatalysts: A comparative study. *Sep. Purif. Technol.* 245, 116892.
- Ahmad, Munir, Qureshi, Muhammad Tauseef, Rehman, Wajid, Alotaibi, Nouf H., Gul, Anadil, Hameed, Reda S. Abdel, Al Elaimi, Mahmoud, Abd El-kader, MFH, Nawaz, Muhammad, Ullah, Rizwan, 2022. Enhanced photocatalytic degradation of RhB dye from aqueous solution by biogenic catalyst Ag@ ZnO. *J. Alloys Compd.* 895, 162636.
- Akbari, Mohammad Zahir, Xu, Yifeng, Liang, Chuanzhou, Lu, Zhikun, Shen, Siyuan, Peng, Lai, 2023. Synthesis of ZnO@ VC for enhancement of synergic photocatalytic degradation of SMX: Toxicity assessment, kinetics and transformation pathway determination. *Chem. Eng. Process. Intensif.* 193, 109544.
- Alansi, Amani M., Qahtan, Talal F., Al Abass, Nawal, Al-Qunaibit, Maha, Saleh, Tawfik A., 2022. In-situ sunlight-driven tuning of photo-induced electron-hole generation and separation rates in bismuth oxychlorobromide for highly efficient water decontamination under visible light irradiation. *J. Colloid Interface Sci.* 614, 58–65.
- Alharthi, Fahad A., Alghamdi, Abdulaziz Ali, Al-Zaqri, Nabil, Alanazi, Hamdah S., Alsyaifi, Amjad Abdullah, Marghany, Adel El, Ahmad, Naushad, 2020. Facile one-pot green synthesis of Ag-ZnO nanocomposites using potato peeland their Ag concentration dependent photocatalytic properties. *Sci. Rep.* 10 (1), 20229.
- Buengkitcharoen, Lalita, Amnuaypanich, Sittipong, Naknonhan, Suriyabhorn, Loiha, Sirinuch, Padthanagul, Nophasinthu, Makdee, Ammarika, Amnuaypanich, Sujitra, 2023. Facile synthesis of robust Ag/ZnO composites by sol-gel auto-combustion and ion-impregnation for the photocatalytic degradation of sucrose. *Sci. Rep.* 13 (1), 12173.
- Cerrón-Calle, Gabriel Antonio, Aranda-Aguirre, Alejandro Junior, Luyo, Clemente, García-Segura, Sergi, Alarcón, Hugo, 2019. Photoelectrocatalytic decolorization of azo dyes with nano-composite oxide layers of ZnO nanorods decorated with Ag nanoparticles. *Chemosphere* 219, 296–304.
- Chankhanitha, Tammanoon, Komchoo, Naputsawan, Senasu, Teeradech, Piriyanon, Jirayus, Youngne, Sujitra, Hemavibool, Khuanjit, Nan, Suwat, 2021. Silver decorated ZnO photocatalyst for effective removal of reactive red azo dye and ofloxacin antibiotic under solar light irradiation. *Colloids Surf. A* 626, 127034.
- Chen, Shuoyu, Bi, Tengfei, Du, Zhenxi, Luo, Shenghao, Fu, Yuechun, He, Huan, Shen, Xiaoming, 2024. Enhanced visible-light photocatalysis in three-dimensional rose-like ZnO with oxygen vacancies and Ag nanoparticles. *New J. Chem.* 48 (2), 910–919.
- Cheng, Xin, Cheng, Zihang, Jing, Binghua, Ao, Zhimin, Shang, Chii, Ling, Li, 2023. Visible light-driven NH₂Cl activation by g-C₃N₄ photocatalysis producing reactive nitrogen species to degrade bisphenol A. *Water Res.* 235, 119889.
- de Albuquerque, Félícia Pereira, de Oliveira, Jhones Luiz, Moschini-Carlos, Viviane, Fraceto, Leonardo Fernandes, 2020. An overview of the potential impacts of atrazine in aquatic environments: perspectives for tailored solutions based on nanotechnology. *Sci. Total Environ.* 700, 134868.
- Deebansok, Siraphrapha, Amornsakchai, Taweechai, Sae-Ear, Pannagorn, Siriphannnon, Punnamra, Smith, Siwaporn Meejoo, 2021. Sphere-like and flake-like ZnO immobilized on pineapple leaf fibers as easy-to-recover photocatalyst for the degradation of congo red. *J. Environ. Chem. Eng.* 9 (2), 104746.
- Dhiman, Pooja, Kumar, Amit, Shekh, Mehdihasan, Sharma, Gaurav, Rana, Garima, Vo, Dai-Viet N., AlMasoud, Najla, Naushad, Mu, ALOthman, Zeid A., 2021. Robust magnetic ZnO-Fe₂O₃ Z-scheme heterojunctions with in-built metal-redox for high performance photo-degradation of sulfamethoxazole and electrochemical dopamine detection. *Environ. Res.* 197, 111074.
- van Dijk, Joanne, Dekker, Stefan C., Kools, Stefan A.E., van Wezel, Annemarie P., 2023. European-wide spatial analysis of sewage treatment plants and the possible benefits to nature of advanced treatment to reduce pharmaceutical emissions. *Water Res.* 241, 120157.
- Dong, Chencheng, Fang, Wenzhang, Yi, Qiuying, Zhang, Jinlong, 2022. A comprehensive review on reactive oxygen species (ROS) in advanced oxidation processes (AOPs). *Chemosphere* 308, 136205.
- El Golli, Asma, Fendrich, Murilo, Bazzanella, Nicola, Dridi, Chérif, Miotello, Antonio, Orlandi, Michele, 2021. Wastewater remediation with ZnO photocatalysts: green synthesis and solar concentration as an economically and environmentally viable route to application. *J. Environ. Manag.* 286, 112226.
- Fatima, Hira, Azhar, Muhammad Rizwan, Zhong, Yijun, Arafat, Yasir, Khiadani, Mehdi, Shao, Zongping, 2022. Rational design of ZnO-zeolite imidazole hybrid nanoparticles with reduced charge recombination for enhanced photocatalysis. *J. Colloid Interface Sci.* 614, 538–546.
- Fekadu, Samuel, Alemayehu, Esayas, Dewil, Raf, Van der Bruggen, Bart, 2019. Pharmaceuticals in freshwater aquatic environments: A comparison of the african and European challenge. *Sci. Total Environ.* 654, 324–337.
- Feng, Chang, Chen, Zhuoyuan, Jing, Jiangping, Hou, Jian, 2020. The photocatalytic phenol degradation mechanism of Ag-modified ZnO nanorods. *J. Mater. Chem. C* 8 (9), 3000–3009.
- Gerbreiders, Vjaceslav, Krasovska, Marina, Sledevskis, Eriks, Gerbreiders, Andrejs, Mihailova, Irena, Tamanis, Edmunds, Ogurcovs, Andrejs, 2020. Hydrothermal synthesis of ZnO nanostructures with controllable morphology change. *CrystEngComm* 22 (8), 1346–1358.

- Ghos, Bijoy Chandra, Farhad, Syed Farid Uddin, Patwary, Md Abdul Majed, Majumder, Shanta, Hossain, Md Alauddin, Tanvir, Nazmul Islam, Rahman, Mohammad Atiqur, Tanaka, Tooru, Guo, Qixin, 2021. Influence of the substrate, process conditions, and postannealing temperature on the properties of ZnO thin films grown by the successive ionic layer adsorption and reaction method. *ACS Omega* 6 (4), 2665–2674.
- Guo, Yefei, Fu, Xiaonan, Xie, Ying, Zhu, Lin, Liu, Ruijie, Liu, Lixin, 2022. Synthesis of Ag/ZnO nanocomposites with enhanced visible photocatalytic performance. *Opt. Mater.* 133, 112980.
- Guo, Zhongyu, Kodikara, Dilini, Albi, Luthfia Shofi, Hatano, Yuta, Chen, Guo, Yoshimura, Chihiro, Wang, Jieqiong, 2023. Photodegradation of organic micropollutants in aquatic environment: Importance, factors and processes. *Water Res.* 231, 118236.
- Khan, Muhammad Zaman, Miltky, Jiri, Baheti, Vijay, Fijalkowski, Mateusz, Wiener, Jakub, Voleský, Lukáš, Adach, Kinga, 2020. Growth of ZnO nanorods on cotton fabrics via microwave hydrothermal method: effect of size and shape of nanorods on superhydrophobic and UV-blocking properties. *Cellulose* 27, 10519–10539.
- Kim, Seok, Lee, Jinseo, Jeong, Nahyeon, Ahn, Yong-Yoon, Kim, Hyeonjeong, Cho, Kangwoo, 2024. Electrochemical UV/Ozone process with Ni-Sb-SnO₂/SiO_x anode for degradation of micropollutants in wastewater. *Chem. Eng. J.* 491, 152018.
- Kusiak-Nejman, E., Wojnarowicz, J., Morawski, A.W., Narkiewicz, U., Sobczak, K., Gierlotka, S., Lojkowski, W., 2021. Size-dependent effects of ZnO nanoparticles on the photocatalytic degradation of phenol in a water solution. *Appl. Surf. Sci.* 541, 148416.
- Le, Anh Thi, Le, Thi Duy Hanh, Cheong, Kuan-Yew, Pung, Swee-Yong, 2022. Immobilization of zinc oxide-based photocatalysts for organic pollutant degradation: A review. *J. Environ. Chem. Eng.* 10 (5), 108505.
- Lee, Kian Mun, Lai, Chin Wei, Ngai, Koh Sing, Juan, Joon Ching, 2016. Recent developments of zinc oxide based photocatalyst in water treatment technology: A review. *Water Res.* 88, 428–448.
- Li, Rui, Kadrispahic, Haris, Jørgensen, Mads Koustrup, Berg, Sisse Brøndum, Thorberg, Dines, Mielczarek, Artur Tomasz, Bester, Kai, 2022a. Removal of micropollutants in a ceramic membrane bioreactor for the post-treatment of municipal wastewater. *Chem. Eng. J.* 427, 131458.
- Li, Bingyan, Kim, Ick Soo, Dai, Shenhua, Sarwar, Muhammad Nauman, Yang, Xuhong, 2021a. Heterogeneous Ag@ZnO nanorods decorated on polyacrylonitrile fiber membrane for enhancing the photocatalytic and antibacterial properties. *Colloid Interface Sci Commun.* 45, 100543.
- Li, Heping, Liu, Jianxing, Wang, Chao, Yang, He, Xue, Xiangxin, 2022b. Oxygen vacancies-enriched and porous hierarchical structures of ZnO microspheres with improved photocatalytic performance. *Vacuum* 199, 110891.
- Li, Yanan, Lu, Qiuyun, Gamal El-Din, Mohamed, Zhang, Xuehua, 2023. Immobilization of photocatalytic ZnO nanocaps on planar and curved surfaces for the photodegradation of organic contaminants in water. *ACS ES&T Water* 3 (8), 2740–2752.
- Li, Ling, Niu, Xiaojun, Zhang, Dongqing, Ye, Xinyao, Zhang, Zhilin, Liu, Qiang, Ding, Lei, Chen, Kun, Chen, Yang, Chen, Kunyang, et al., 2024. A systematic review on percarbonate-based advanced oxidation processes in wastewater remediation: From theoretical understandings to practical applications. *Water Res.* 121842.
- Li, Shao-Hai, Qi, Ming-Yu, Tang, Zi-Rong, Xu, Yi-Jun, 2021b. Nanostructured metal phosphides: from controllable synthesis to sustainable catalysis. *Chem. Soc. Rev.* 50 (13), 7539–7586.
- Lin, Wei, Liu, Xiao, Ding, An, Ngo, Huu Hao, Zhang, Rourou, Nan, Jun, Ma, Jun, Li, Guibai, 2022. Advanced oxidation processes (AOPs)-based sludge conditioning for enhanced sludge dewatering and micropollutants removal: A critical review. *J. Water Process Eng.* 45, 102468.
- Liu, Qiong, Liu, Ertao, Li, Ju, Qiu, Yuan, Chen, Rong, 2020. Rapid ultrasonic-microwave assisted synthesis of spindle-like Ag/ZnO nanostructures and their enhanced visible-light photocatalytic and antibacterial activities. *Catalysis Today* 339, 391–402.
- Liu, Yangsi, Wei, Shanghai, Gao, Wei, 2015. Ag/ZnO heterostructures and their photocatalytic activity under visible light: effect of reducing medium. *J. Hazard. Mater.* 287, 59–68.
- López, Rosendo, Gómez, Ricardo, 2012. Band-gap energy estimation from diffuse reflectance measurements on sol-gel and commercial TiO₂: a comparative study. *J. Sol-Gel Sci. Technol.* 61, 1–7.
- Lu, Qiuyun, Khanna, Pranav, Chelme-Ayala, Pamela, Xu, Ben Bin, Gamal El-Din, Mohamed, Zhang, Xuehua, 2024. Scalable and facile formation of microlenses on curved surfaces enabling a highly customized sustainable solar-water nexus. *Small Struct.* 5 (2), 2300238.
- Luo, Sha, Liu, Chunwei, Wan, Yang, Li, Wei, Ma, Chunhui, Liu, Shouxin, Heeres, Hero Jan, Zheng, Weiqing, Seshan, Kulathuwyer, He, Songbo, 2020a. Self-assembly of single-crystal ZnO nanorod arrays on flexible activated carbon fibers substrates and the superior photocatalytic degradation activity. *Appl. Surf. Sci.* 513, 145878.
- Luo, Sha, Liu, Chunwei, Zhou, Sui, Li, Wei, Ma, Chunhui, Liu, Shouxin, Yin, Wang, Heeres, Hero Jan, Zheng, Weiqing, Seshan, Kulathuwyer, et al., 2020b. ZnO nanorod arrays assembled on activated carbon fibers for photocatalytic degradation: Characteristics and synergistic effects. *Chemosphere* 261, 127731.
- Luo, Yidan, Zheng, Aofeng, Li, Junda, Han, Yu, Xue, Mingshan, Zhang, Longshuai, Yin, Zuozhu, Xie, Chan, Chen, Zhi, Ji, Li, et al., 2023. Integrated adsorption and photodegradation of tetracycline by bismuth oxycarbonate/biochar nanocomposites. *Chem. Eng. J.* 457, 141228.
- Ma, Xinlong, Li, Hao, Liu, Tongyao, Du, Shanshan, Qiang, Qinping, Wang, Yuhua, Yin, Shu, Sato, Tsugio, 2017. Comparison of photocatalytic reaction-induced selective corrosion with photocorrosion: Impact on morphology and stability of Ag-ZnO. *Appl. Catal. B* 201, 348–358.
- Maeng, Sung Kyu, Cho, Kangwoo, Jeong, Boyoung, Lee, Jaesang, Lee, Yunho, Lee, Changha, Choi, Kyoung Jin, Hong, Seok Won, 2015. Substrate-immobilized electrospun TiO₂ nanofibers for photocatalytic degradation of pharmaceuticals: The effects of pH and dissolved organic matter characteristics. *Water Res.* 86, 25–34.
- Mahrsi, Mouna Ibn, Chouchene, Bilel, Gries, Thomas, Carré, Vincent, Girot, Emilien, Medjahdi, Ghouti, Ayari, Fadila, Balan, Lavinia, Schneider, Raphaël, 2023. Novel ZnO/Ag nanohybrids prepared from Ag⁺-doped layered zinc hydroxides as highly active photocatalysts for the degradation of dyes and ciprofloxacin. *Colloids Surf. A* 671, 131643.
- Makropoulou, Tatiana, Kortidis, Ioannis, Davididou, Konstantina, Motaung, David E., Chatzisymeon, Efthalia, 2020. Photocatalytic facile ZnO nanostructures for the elimination of the antibiotic sulfamethoxazole in water. *J. Water Process Eng.* 36, 101299.
- Mirzaei, Amir, Yerushalmi, Laleh, Chen, Zhi, Haghishat, Fariborz, 2018a. Photocatalytic degradation of sulfamethoxazole by hierarchical magnetic ZnO@g-C₃N₄: RSM optimization, kinetic study, reaction pathway and toxicity evaluation. *J. Hazard. Mater.* 359, 516–526.
- Mirzaei, Amir, Yerushalmi, Laleh, Chen, Zhi, Haghishat, Fariborz, Guo, Jianbo, 2018b. Enhanced photocatalytic degradation of sulfamethoxazole by zinc oxide photocatalyst in the presence of fluoride ions: Optimization of parameters and toxicological evaluation. *Water Res.* 132, 241–251.
- Mohammed, Reem, Ali, Mohamed Eid M., Gomaa, E., Mohsen, M., 2020. Green ZnO nanorod material for dye degradation and detoxification of pharmaceutical wastes in water. *J. Environ. Chem. Eng.* 8 (5), 104295.
- Montero-Muñoz, Marly, Ramos-Ibarra, Jesús Ernesto, Rodríguez-Páez, J.E., Marques, GE, Teodoro, M.D., Coaqueira, JAH, 2020. Growth and formation mechanism of shape-selective preparation of ZnO structures: correlation of structural, vibrational and optical properties. *Phys. Chem. Chem. Phys.* 22 (14), 7329–7339.
- Mou, Hongyu, Song, Caixia, Zhou, Yanhong, Zhang, Bo, Wang, Debao, 2018. Design and synthesis of porous Ag/ZnO nanosheets assemblies as super photocatalysts for enhanced visible-light degradation of 4-nitrophenol and hydrogen evolution. *Appl. Catal. B* 221, 565–573.
- Muñoz-Fernandez, Lidia, Gómez-Villalba, Luz Stella, Milošević, Olivera, Rabanal, María Eugenia, 2022. Influence of nanoscale defects on the improvement of photocatalytic activity of Ag/ZnO. *Mater. Charact.* 185, 111718.
- Pham, Thi Anh Tuyet, Tran, Van Anh, Le, Van Duong, Nguyen, Minh Viet, Truong, Duc Duc, Do, Xuan Truong, Vu, Anh-Tuan, 2020. Facile preparation of ZnO nanoparticles and Ag/ZnO nanocomposite and their photocatalytic activities under visible light. *Int. J. Photoenergy* 2020 (1), 8897667.
- Qi, Ming-Yu, Conte, Marco, Anpo, Masakazu, Tang, Zi-Rong, Xu, Yi-Jun, 2021. Cooperative coupling of oxidative organic synthesis and hydrogen production over semiconductor-based photocatalysts. *Chem. Rev.* 121 (21), 13051–13085.
- Qiu, Yu, Yu, Shan, Wang, Song-Meng, Liu, Mei-Ling, Li, Shi-Yao, Yao, Huan, Yang, Liu-Pan, Wang, Li-Li, 2024. Adaptive tetralactam macrocycle based polymers for efficient and rapid removal of organic micropollutants with wide scope. *Chem. Eng. J.* 153143.
- Rabell, G., Ortiz, Cruz, M.R., Alfaro, Juárez-Ramírez, I., 2021. Hydrogen production of ZnO and ZnO/Ag films by photocatalysis and photoelectrocatalysis. *Mater. Sci. Semicond. Process.* 134, 105985.
- Ramasamy, Bhuvaneswari, Jeyadharmarajan, Jeyanthi, Chinnaian, Prakash, 2021. Novel organic assisted Ag-ZnO photocatalyst for atenolol and acetaminophen photocatalytic degradation under visible radiation: performance and reaction mechanism. *Environ. Sci. Pollut. Res.* 28 (29), 39637–39647.
- Rana, Anchal, Sudhaik, Anita, Raizada, Pankaj, Nguyen, Van-Huy, Xia, Changlei, Khan, Aftab Aslam Parwaz, Thakur, Sourbh, Nguyen-Tri, Phuong, Nguyen, Chinh Chien, Kim, Soo Young, et al., 2022. Graphitic carbon nitride based immobilized and non-immobilized floating photocatalysts for environmental remediation. *Chemosphere* 297, 134229.
- Rodríguez-González, Vicente, Obregón, Sergio, Patrón-Soberano, Olga A., Terashima, Chiaki, Fujishima, Akira, 2020. An approach to the photocatalytic mechanism in the TiO₂-nanomaterials microorganism interface for the control of infectious processes. *Appl. Catal. B* 270, 118853.
- Roy, Namrata, Kannabiran, Krishnan, Mukherjee, Amitava, 2023. Integrated adsorption and photocatalytic degradation based removal of ciprofloxacin and sulfamethoxazole antibiotics using Fc@rGO-ZnO nanocomposite in aqueous systems. *Chemosphere* 333, 138912.
- Shabannia, R., 2016. Effects of growth duration and precursor concentration on the growth of ZnO nanorods synthesized by chemical bath deposition. *Iran. J. Sci. Technol. Trans. A Sci.* 40, 19–25.
- Shang, Feng-Kang, Li, Yue-Hua, Qi, Ming-Yu, Tang, Zi-Rong, Xu, Yi-Jun, 2023. Photocatalytic materials for sustainable chemistry via cooperative photoredox catalysis. *Catalysis Today* 410, 85–101.

- Shen, Jyun-Hong, Chiang, Tzu-Hui, Tsai, Cheng-Kuo, Jiang, Zhu-Wu, Horng, Jao-Jia, 2022. Mechanistic insights into hydroxyl radical formation of Cu-doped ZnO/g-C₃N₄ composite photocatalysis for enhanced degradation of ciprofloxacin under visible light: Efficiency, kinetics, products identification and toxicity evaluation. *J. Environ. Chem. Eng.* 10 (2), 107352.
- Sher, Farooq, Hanif, Kashif, Rafey, Abdul, Khalid, Ushna, Zafar, Ayesha, Ameen, Mariam, Lima, Eder C., 2021. Removal of micropollutants from municipal wastewater using different types of activated carbons. *J. Environ. Manag.* 278, 111302.
- Singh, Sarika, 2022. Natural sunlight driven photocatalytic performance of Ag/ZnO nanocrystals. *Mater. Today Commun.* 33, 104438.
- Singh, Adarsh, Majumder, Abhradeep, Saidulu, Duduku, Bhattacharya, Animesh, Bhattacharya, Amit, Gupta, Ashok Kumar, 2024. Oxidative treatment of micropollutants present in wastewater: A special emphasis on transformation products, their toxicity, detection, and field-scale investigations. *J. Environ. Manag.* 354, 120339.
- Su, Ruidian, Zhu, Yongfa, Gao, Baoyu, Li, Qian, 2024. Progress on mechanism and efficacy of heterogeneous photocatalysis coupled oxidant activation as an advanced oxidation process for water decontamination. *Water Res.* 121119.
- Tan, Huey Jing, Zainal, Zulkarnain, Talib, Zainal Abidin, Lim, Hong Ngee, Shafee, Suhaidi, Tan, Sin Tee, Tan, Kar Ban, Bahrudin, Noor Nazihah, 2021. Synthesis of high quality hydrothermally grown ZnO nanorods for photoelectrochemical cell electrode. *Ceram. Int.* 47 (10), 14194–14207.
- Tang, Xiangwei, Tang, Rongdi, Xiong, Sheng, Zheng, Jiangfu, Li, Ling, Zhou, Zhanpeng, Gong, Daoxin, Deng, Yaocheng, Su, Long, Liao, Chanjuan, 2022. Application of natural minerals in photocatalytic degradation of organic pollutants: A review. *Sci. Total Environ.* 812, 152434.
- Vaiano, Vincenzo, Iervolino, Giuseppina, 2018. Facile method to immobilize ZnO particles on glass spheres for the photocatalytic treatment of tannery wastewater. *J. Colloid Interface Sci.* 518, 192–199.
- Vinh, Tran Hoang The, Thuy, Nguyen Thi Be, Thi, Cao Minh, Van Viet, Pham, et al., 2021. Visible-light-driven photocatalysis of anisotropic silver nanoparticles decorated on ZnO nanorods: Synthesis and characterizations. *J. Environ. Chem. Eng.* 9 (2), 105103.
- Wang, Chih-Chiang, Shieh, Fuh-Sheng, Shih, Han C., 2021. Ag-nanoparticle enhanced photodegradation of ZnO nanostructures: Investigation using photoluminescence and ESR studies. *J. Environ. Chem. Eng.* 9 (1), 104707.
- Wei, Zixiang, Dabodiya, Tulsi Satyavir, Chen, Jian, Lu, Qiuyun, Qian, Jiasheng, Meng, Jia, Zeng, Hongbo, Qian, Hui, Zhang, Xuehua, 2022. In-situ fabrication of metal oxide nanocaps based on biphasic reactions with surface nanodroplets. *J. Colloid Interface Sci.* 608, 2235–2245.
- Wu, Hao, Irani, Rowshanak, Zhang, Kunfeng, Jing, Lin, Dai, Hongxing, Chung, Hoi Ying, Abdi, Fatwa F., Ng, Yun Hau, 2021. Unveiling carrier dynamics in periodic porous b₂VO₄ photocatalyst for enhanced solar water splitting. *ACS Energy Lett.* 6 (10), 3400–3407.
- Xie, Zhiqun, Saad, Ali, Shang, Yanan, Wang, Yong, Luo, Shuang, Wei, Zongsu, 2023. Enhanced degradation of micropollutants by visible light photocatalysts with strong oxygen activation ability. *Water Res.* 247, 120785.
- Xu, Mingming, An, Yangjuan, Wang, Qianqian, Wang, Junmin, Hao, Lin, Wang, Chun, Wang, Zhi, Zhou, Junhong, Wu, Qiuhua, 2021. Construction of hydroxyl functionalized magnetic porous organic framework for the effective detection of organic micropollutants in water, drink and cucumber samples. *J. Hazard. Mater.* 412, 125307.
- Yang, Tao, An, Linqian, Zeng, Ge, Mai, Jiamin, Li, Yuying, Lian, Jinchuan, Zhang, Haochen, Li, Juan, Cheng, Xiaoxiang, Jia, Jianbo, et al., 2023. Enhanced hydroxyl radical generation for micropollutant degradation in the In₂O₃/Vis-LED process through the addition of periodate. *Water Res.* 243, 120401.
- Yang, Lei, Bai, Xue, Shi, Juan, Du, Xinyu, Xu, Lu, Pengkang, 2019. Quasi-full-visible-light absorption by D35-TiO₂/g-C₃N₄ for synergistic persulfate activation towards efficient photodegradation of micropollutants. *Appl. Catal. B* 256, 117759.
- Young, Sheng-Joue, Chu, Yu-Jhih, Chen, Yu-Long, 2021. Enhancing pH sensors performance of ZnO nanorods with Au nanoparticles adsorption. *IEEE Sens. J.* 21 (12), 13068–13073.
- Yuan, Junwei, Li, Hua, Wang, Guan, Zhang, Cheng, Wang, Yuxiang, Yang, Liujun, Li, Miaomiao, Lu, Jianmei, 2022. Adsorption, isolated electron/hole transport, and confined catalysis coupling to enhance the photocatalytic degradation performance. *Appl. Catal. B* 303, 120892.
- Zamiri, Reza, Rebelo, Avito, Zamiri, Golriz, Adnani, Atena, Kuashal, Ajay, Belsley, Michael Scott, Ferreira, J.M.F., 2014. Far-infrared optical constants of ZnO and ZnO/Ag nanostructures. *RSC Adv.* 4 (40), 20902–20908.
- Zandsalimi, Yahya, Maleki, Afshin, Shahmoradi, Behzad, Dehestani, Saeed, Rezaee, Reza, McKay, Gordon, 2022. Photocatalytic removal of 2, 4-Dichlorophenoxyacetic acid from aqueous solution using tungsten oxide doped zinc oxide nanoparticles immobilised on glass beads. *Environ. Technol.* 43 (5), 631–645.
- Zhang, Caijian, Jia, Meiyi, Xu, Zhengyong, Xiong, Weiping, Yang, Zhaohui, Cao, Jiao, Peng, Haihao, Xu, Haiyin, Xiang, Yingping, Jing, Ying, 2022a. Constructing 2D/2D N-ZnO/g-C₃N₄ S-scheme heterojunction: efficient photocatalytic performance for norfloxacin degradation. *Chem. Eng. J.* 430, 132652.
- Zhang, Fan, Li, Yue-Hua, Li, Jing-Yu, Tang, Zi-Rong, Xu, Yi-Jun, 2019a. 3D graphene-based gel photocatalysts for environmental pollutants degradation. *Environ. Pollut.* 253, 365–376.
- Zhang, Lin, Li, Nuomei, Ma, Qiuchen, Ding, Jiahui, Chen, Chuang, Hu, Zhaocheng, Zhao, Weiwei, Li, Yufeng, Feng, Huanhuan, Li, Mingyu, et al., 2022b. Large-area flexible and transparent UV photodetector based on cross-linked Ag NW@ZnO NRs with high performance. *J. Mater. Sci. Technol.* 110, 65–72.
- Zhang, Fan, Li, Yue-Hua, Qi, Ming-Yu, Tang, Zi-Rong, Xu, Yi-Jun, 2020a. Boosting the activity and stability of Ag-Cu₂O/ZnO nanorods for photocatalytic CO₂ reduction. *Appl. Catal. B* 268, 118380.
- Zhang, Yizhen, Liu, Lifen, Van der Bruggen, Bart, Leung, Michael K.H., Yang, Fenglin, 2019b. A free-standing 3D nano-composite photo-electrode-Ag/ZnO nanorods arrays on Ni foam effectively degrade berberine. *Chem. Eng. J.* 373, 179–191.
- Zhang, Xuehua, Lu, Ziyang, Tan, Huanshu, Bao, Lei, He, Yinghe, Sun, Chao, Lohse, Detlef, 2015. Formation of surface nanodroplets under controlled flow conditions. *Proc. Natl. Acad. Sci.* 112 (30), 9253–9257.
- Zhang, Yong, Zhai, Guangmei, Gao, Lingwei, Chen, Qing, Ren, Jintao, Yu, Jun, Yang, Yongzhen, Hao, Yuying, Liu, Xuguang, Xu, Bingshe, et al., 2020b. Improving performance of perovskite solar cells based on ZnO nanorods via rod-length control and sulfidation treatment. *Mater. Sci. Semicond. Process.* 117, 105205.
- Zheng, Haorong, Jiang, Yurong, Yang, Shengyi, Zhang, Yong, Yan, Xuefeng, Hu, Jining, Shi, Yuansheng, Zou, Bingsuo, 2020. ZnO nanorods array as light absorption antenna for high-gain UV photodetectors. *J. Alloys Compd.* 812, 152158.